JOURNAL OF GEOPHYSICAL RESEARCH, VOL. 104, NO. C3, PAGES 5191–5209, MARCH 15, 1999

Mass, heat, and salt transport in the southeastern Pacific: A Circumpolar Current inverse model

Sarah T. Gille

Department of Earth System Science, University of California, Irvine

Abstract. A box inverse model for the southeastern Pacific is used to combine hydrographic measurements with synoptic information from floats, acoustic Doppler surface velocity measurements, altimeter-derived surface geostrophic velocities, and wind measurements. The southeastern Pacific is marked by substantial changes in eddy kinetic energy along the path of the Antarctic Circumpolar Current (ACC), associated with the Eltanin and Udintsev Fracture Zones in the East Pacific Rise. The results of the inverse model show that the heat and salt carried by the ACC are essentially unchanged as the current passes through regions of high eddy variability. Thus, within the error bars of the available measurements the ACC appears not to exchange significant water properties with its surroundings in the southeastern Pacific Ocean. (The system is geographically variable, and elsewhere in the Southern Ocean, meridional exchanges may be substantial.) Meridional flow through the north side of the inverse model domain is consistent with an overturning circulation that carries surface intermediate water northward and returns deep water southward into the ACC. Diapycnal fluxes identified in the inverse solution indicate that water mass transformation occurs predominantly in the outcropping upper layers of the ocean.

1. Introduction

The Antarctic Circumpolar Current (ACC) is the oceanic link between the Atlantic, Indian, and Pacific Oceans. Estimated to have an eastward transport of $130 \pm 15 \times 10^6$ m^3 s^{-1} [*Whitworth et al.*, 1982], the ACC is large enough to influence global mass and heat budgets. Its influence on climate processes depends both on air-sea fluxes and on the meridional exchange processes that link the circumpolar flow with the subtropical ocean circulation in each of the three basins and with the Antarctic continental margins.

Studies based on atmospheric and oceanic observations indicate that the global ocean carries 1 to 2 PW southward into the Southern Ocean at 40°S [*Talley*, 1984; *Hsiung*, 1985] and between 0.3 and 0.7 PW southward across the ACC [*Gordon and Owens*, 1987; *Keffer and Holloway*, 1988]. Basin-scale analyses of the Southern Ocean heat budget suggest that this southward meridional heat transport is concentrated in the Indian Ocean [*Georgi and Toole*, 1982; *Macdonald and Wunsch*, 1996; *Sloyan*, 1997]. *Georgi and Toole* [1982] estimated the meridional heat exchange between the three oceans and the ACC by examining hydrographic sections across each of the three choke points of the Circumpolar Current. They observed that the mean temperature of water transported across each of the three sections was coldest south of Africa and warmest south of New Zealand, implying that the ACC warmed in the Indian sector and cooled in the Pacific and Atlantic sectors of the Southern Ocean. *Macdonald and Wunsch* [1996] obtained similar results in a global inverse model as did *Sloyan* [1997] for a Southern Ocean inverse model: heat transport across meridional lines transecting the Southern Ocean was lowest south of Africa and highest south of Australia. Correspondingly, meridional heat transport estimates implied southward heat flow in the Indian Ocean and northward heat transport in the Pacific and Atlantic Oceans.

Past studies were not designed to look at how the heat transported by the ACC varied over distances smaller than the basin scale, and they did not analyze the advective and diffusive processes that account for meridional heat exchange. Since the Southern Ocean is a region of high eddy kinetic energy, as indicated in altimeter measurements [e.g., *Sandwell and Zhang*, 1989], we might hypothesize that mesoscale eddies are responsible for mixing heat between the subtropics and the Circumpolar Current. This view is supported by earlier work based on hydrographic data: *deSzoeke and Levine* [1981] considered a coordinate system in which there was no time-mean advective heat flux across the ACC. Therefore they conjectured that eddy processes must balance both the heat lost to the atmosphere south of the ACC ($\sim$ 0.3 PW) and the heat advected northward by the surface Ekman transport ($\sim$ 0.15 PW).

Keffer and Holloway [1988] suggested that eddy diffusivity should be proportional to root-mean-squared (rms) sea surface height (SSH), while *Stammer* [1998] explored the possibility that diffusivity is proportional to surface eddy kinetic energy (EKE). Along the path of the ACC, rms SSH

Paper number 1998JC900106.
0148-0227/99/1998JC900106$09.00

and EKE both vary by a factor of 10 on 1000-km length scales. These variations imply geographical differences in the diffusion coefficients and, correspondingly, suggest that the eddy-induced heat transfer southward across the ACC might be localized in the regions of highest EKE.

While eddy mixing offers a plausible explanation for the meridional heat transport into the Southern Ocean, the ACC itself may act as a barrier to heat exchange. The current is made up of narrow frontal jets [*Orsi et al.*, 1995] that are distinguished by outcropping isopycnals. Since mixing in the ocean is often presumed to occur more rapidly along isopycnals than across isopycnals, these outcropping surfaces may prevent high meridional heat transport, even when there is high eddy activity.

This paper examines the mass, heat, and salt transport of the ACC through five meridional sections in the southeastern Pacific carried out as part of the World Ocean Circulation Experiment (WOCE). The hydrographic data delineate four boxes (Figure 1) and include regions with large topography and with high eddy activity downstream of topography as well as relatively quiescent midbasin conditions (see Figure 2), allowing us not only to assess the ACC volume, heat, and salt transport but also to consider whether moderately varying levels of eddy activity influence the heat budget.

To determine reference velocities for the hydrographic data, a box inverse model is developed much like the ones described by *Rintoul* [1991] for the South Atlantic and by *Macdonald and Wunsch* [1996] for the global ocean. The inverse model is constrained not only by hydrographic measurements but also by ancillary measurements carried out as part of the WOCE program, including shipboard acoustic Doppler current profiler (ADCP), Autonomous Lagrangian Circulation Explorer (ALACE) floats, TOPEX satellite altimeter measurements, and ERS-1 satellite scatterometer wind estimates. The results will show that the two primary jets of the ACC carry about 100×10^6 m^3 s^{-1} and 1.2 to 1.3 PW. Within the error bars of the inversion, the enormous changes in eddy kinetic energy in the southeastern Pacific appear to have only minimal impact on the heat content of the ACC. The results also indicate that the vertical structure of the current changes little as it progresses through this region, with most of the heat transport concentrated in upper ocean layers, and that the model supports a small meridional overturning circulation consistent with northward surface flow, deep southward return flow, and upwelling within the ACC.

Section 2 discusses the measurements and error estimates that enter the inverse model while the full details of the inverse model are presented in the appendix. Section 3 presents the results of the inverse model. Section 4 discusses the resulting heat budget as well as the vertical structure of the current, meridional overturning, and the diapycnal fluxes

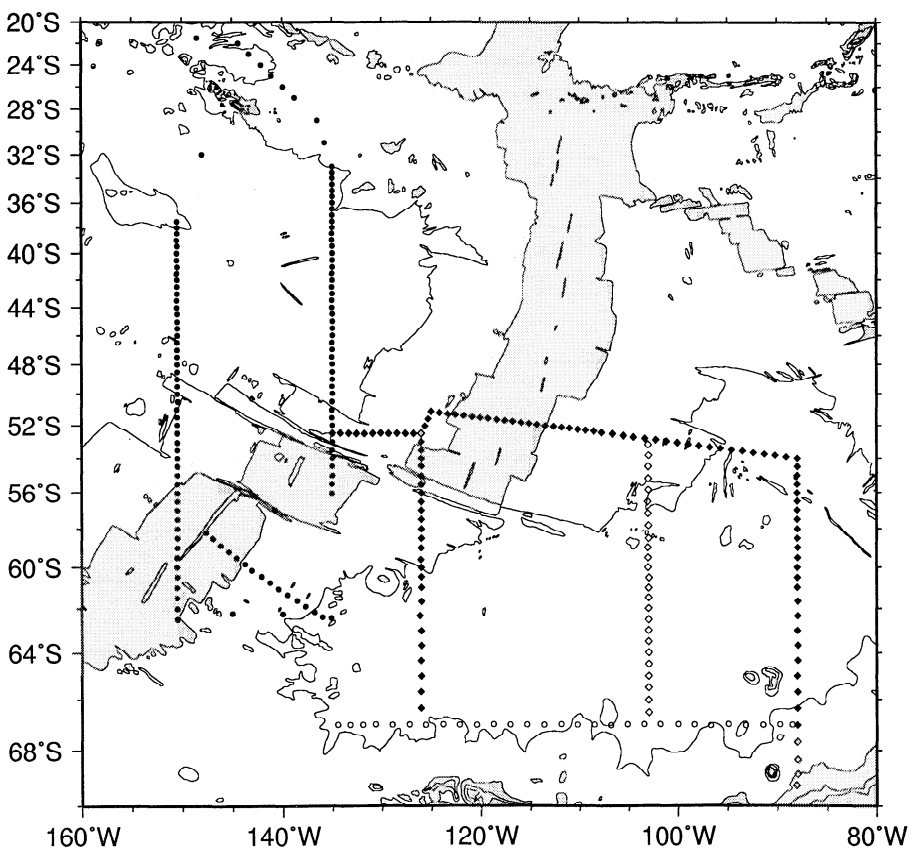

Figure 1. Station locations used in this study from WOCE P16–P17 (solid circles), P17–P19 (solid diamonds), S04 (open circles), and P18 (open diamonds). Stations from P17–P19 that are used in the three-box model F but not in the standard model are shown as shaded diamonds. Bathymetry is contoured at 1000-m intervals, starting at 500 m depth, and regions shallower than 3500 m are shaded.

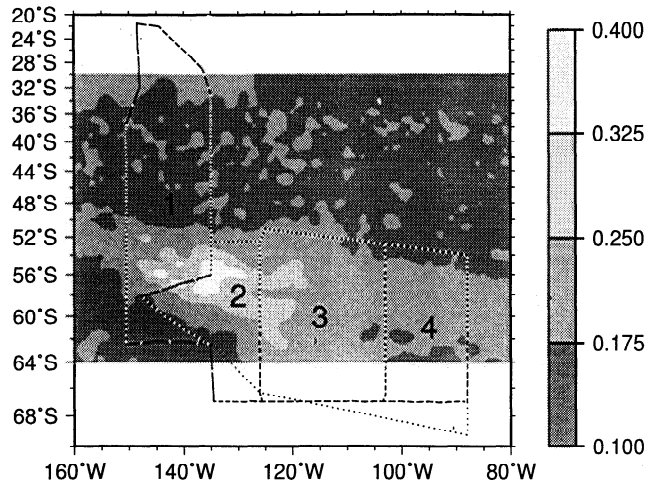

Figure 2. Station midpoints at which hydrographic velocities are computed, shown as open dots. Solid lines delineate the boxes used in the inverse model, and the boxes are numbered from west to east. The shaded background indicates the rms eddy velocity (or square root of eddy kinetic energy) from the TOPEX altimeter in m s^{-1}. The dotted line delineates the southern boundary of the boxes for the three-box model F, in which boxes 3 and 4 are merged.

obtained from the inverse model. Section 5 summarizes the findings.

2. Methodology

This study makes use of an eclectic inverse model, combining all available measurements from the southeastern Pacific WOCE cruises to provide a best estimate of ACC transport through this region. The basic techniques of inverse modeling are discussed in detail by *Wunsch* [1996], and the specifics of the method adopted in this study are presented in the appendix.

2.1. Hydrography

The core of the study is based on hydrographic data from four WOCE cruises, as shown in Figure 1: P16–P17 (October–November 1992), P17–P19 (December 1992 to January 1993), S04 (February–March 1992), and P18 (February–March 1994). The nominal station spacing is about 55 km along WOCE sections. Together these cruises provide a total of 285 station pairs for the standard inverse model, defining four boxes, as shown in Figure 2. In order to minimize the unknown influence of interannual variability, a reduced three-box inverse model is also considered, using only data from the P16–P17 and P17-P19 cruises carried out over a 4-month period in 1992–1993.

Flow is assumed to be in thermal wind balance, with a wind-driven surface Ekman transport in the shallowest ocean layer. In each of the four boxes, mass, temperature, and salt are conserved within error limits, both in the vertically integrated budget and within 18 separate layers.

Layers are defined based on neutral density [*Jackett and McDougall*, 1997; *Sloyan*, 1997] rather than potential density, because isopycnals tilt steeply throughout the Southern Ocean, so that the depth of a layer may vary by 2000 m or more between the northern and southern ends of the domain. Thus there is no single appropriate depth to reference potential density calculations throughout the water column. One resolution to this problem would be to vary the reference depth, so that as an isopycnal rises across the ACC, its potential density is computed with respect to a rising series of reference depths [*Reid*, 1986; *Rintoul*, 1991]. Neutral surfaces provide a consistent and repeatable way of achieving the same effect. Neutral density interfaces are spaced from 26.7 to 28.3 kg m^{-3} at 0.1 kg m^{-3} intervals, as summarized in Table 1. Based on standard watermass definitions, layer 1 represents subtropical surface waters, layers 2–10 correspond to intermediate waters such as Antarctic Intermediate Water and Subantarctic Mode Water, and layers 11–16 typify deep waters including Circumpolar Deep Water, North Atlantic Deep Water, and Pacific Deep Water [*Sloyan*, 1997]. Layers 17 and 18 correspond to bottom water; the mean salinity of 34.70 and relatively warm mean potential temperatures in these southeastern Pacific data are typical of Ross Sea Bottom Water [*Carmack*, 1990]. Figures 3 and 4 show how steeply potential temperature and neutral-density layer depths rise across the ACC in the westernmost and easternmost sections considered in this study.

In the reduced inverse model the boxes do not close tightly in the south, where the ship tracks extended to the ice edge and in both models the northern end of the westernmost box was not extensively sampled. The sparse sampling across the Pacific–Antarctic Ridge, between 147°W, 58°S and 135°W, 56°S, is also potentially troublesome because the ACC transport is large in this area. The large body of ancillary measurements carried out as part of the WOCE research program provide supplemental information to help constrain the inverse calculations.

2.2. Wind Measurements

Surface Ekman transports were determined from gridded weekly wind stresses produced by the French satellite data archiving facility (Centre ERS d'Archivage et de Traitement, CERSAT) [*Bentamy et al.*, 1996]. In these fields, ERS scatterometer winds have been used to improve European Centre for Medium Range Weather Forecasts (ECMWF) operational winds. Shaded vectors in Figure 5 show average wind stress for the 6 months from September 1992 to February 1993, spanning the period when most of the hydrographic measurements were taken. These winds are taken to represent the seasonal mean corresponding to all of the in situ measurements.

Time-averaged wind data, within ±0.6° latitude and within ±1.1° longitude of each hydrographic station midpoint, are averaged to determine mean cross-track wind stresses. Ekman transports are estimated according to

$$fv_E h_E = -\frac{\tau^x}{\rho_o}, \tag{1}$$

where v_E is the cross-track Ekman-induced ageostrophic velocity, h_E is the depth of the Ekman layer, τ^x is the along-

Table 1. Properties on Each of the 18 Neutral Density Levels Used in the Inverse Model.

Layer	Neutral Density	Mean Depth, m	Depth Range, m	$\overline{\sigma}$, kg m^{-3} -1000	$\overline{\theta}$, °C	$\overline{S}$, PSU
1	surface to 26.7	178	0 – 462	σ_0 = 25.6	15.89	35.13
2	26.7 — 26.8	253	0 – 488	σ_0 = 26.6	9.26	34.49
3	26.8 — 26.9	187	0 – 522	σ_0 = 26.7	8.22	34.40
4	26.9 — 27.0	254	0 – 572	σ_0 = 26.8	7.70	34.42
5	27.0 — 27.1	384	0 – 802	σ_0 = 26.8	6.85	34.38
6	27.1 — 27.2	559	0 – 972	σ_1 = 31.6	5.83	34.29
7	27.2 — 27.3	684	0 – 1078	σ_1 = 31.7	4.79	34.24
8	27.3 — 27.4	781	0 – 1202	σ_1 = 31.8	4.09	34.26
9	27.4 — 27.5	846	0 – 1346	σ_1 = 31.9	3.22	34.26
10	27.5 — 27.6	946	0 – 1492	σ_1 = 32.0	2.77	34.32
11	27.6 — 27.7	1111	0 – 1680	σ_1 = 32.1	2.61	34.41
12	27.7 — 27.8	1272	0 – 1904	σ_1 = 32.2	2.43	34.50
13	27.8 — 27.9	1529	120 – 2258	σ_2 = 36.8	2.23	34.59
14	27.9 — 28.0	1978	132 – 2950	σ_2 = 36.9	1.91	34.67
15	28.0 — 28.1	2520	160 – 4630	σ_3 = 41.3	1.47	34.71
16	28.1 — 28.2	3268	354 – 6186	σ_3 = 41.4	0.93	34.72
17	28.2 — 28.3	3489	1310 – 5764	σ_3 = 41.6	0.31	34.70
18	28.3 — bottom	4012	2762 – 5158	σ_4 = 46.1	-0.04	34.70

Mean depth indicates the average depth of water in the neutral density layer. Because isopycnals tilt strongly across the ACC, the depth range for any given neutral surface can be several thousand meters. Values of $\overline{\sigma}$, $\overline{\theta}$, and $\overline{S}$ indicate mean values of potential density, potential temperature, and salinity, respectively, for water in a given neutral density category.

track wind stress, and ρ_o is the ocean density. For the purposes of the inverse model, Ekman transport is always assumed to be contained within the uppermost neutral surface layer at each hydrographic data pair. Solid vectors in Figure 5 indicate the implied upper ocean velocities due to Ekman transport, under the assumption that the Ekman layer is 100 m deep. Since the wind is strongly zonal, the Ekman transport is primarily northward across zonal lines, and the Ekman transport contributes little to the mean ACC transport across the meridional lines.

2.3. ADCP Measurements

As part of the WOCE program, a hull-mounted 153-kHz ADCP system provided estimates of near-surface velocities. Velocity measurements were made in 60 depth bins, centered at 8-m intervals starting 21 m below the surface. Only ADCP measurements from the P16–17 and P17–P19 were considered in this study. For each once-per-second ping, velocities relative to the transducer were rotated to geographical coordinates using the gyro-compass heading and then vector-averaged over 5-min ensembles. Compass errors were estimated from simultaneous heading measurements made by an Ashtech 3DF Global Positioning System (GPS) attitude sensor [*King and Cooper*, 1993], and velocities were corrected for these errors during post processing. Gaps in GPS attitude coverage were filled with a gyro-compass model based on equations 10.36 to 10.39 of *Wrigley et al.* [1969] (P16–P17) or linear interpolation (P17–P19). Additional post-processing used the University of Hawaii CODAS software package [*Firing*, 1991] and regridded the data at 10-m intervals. Standard water track calibration methods [*Joyce*, 1989; *Pollard and Read*, 1989] provided a velocity scale factor and a constant angular offset between transducer and GPS antenna array.

The ADCP measurements were integrated vertically for depth bins centered between 21 m and 311 m and averaged horizontally between stations. This ADCP upper ocean transport was then compared with the geostrophic transport from the same depth range derived from conductivity-temperature-depth (CTD) data and Ekman transport based on winds. The difference between the ADCP transport and

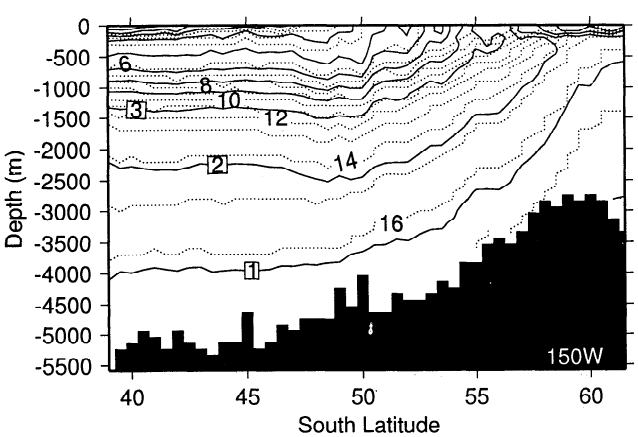

Figure 3. Meridional section of potential temperature (solid lines) and neutral-density layer interfaces (dashed lines) at 150.5°W. Contour intervals are 1°C and 1 kg m^{-3}, respectively. Temperature contour labels are in boxes. Note the significant change in depth of the neutral-density surfaces with latitude.

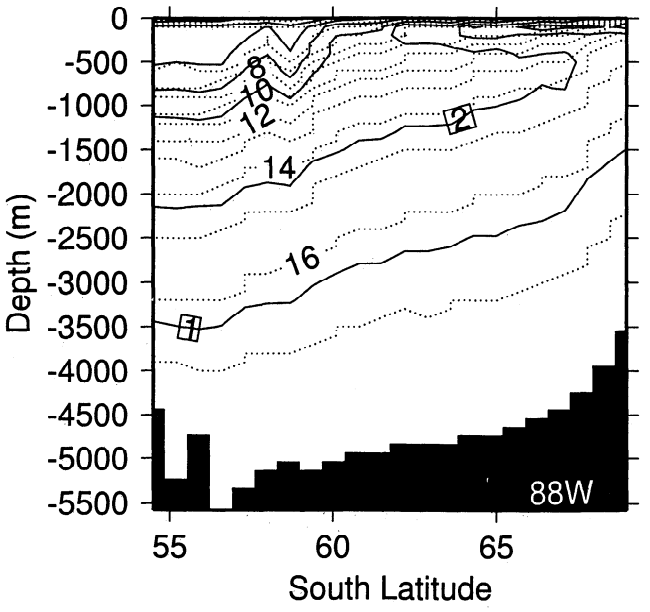

Figure 4. Meridional section of potential temperature (solid lines) and neutral-density layer interfaces (dashed lines) at 88°W, as in Figure 3.

the geostrophic plus Ekman transport is the transport due to the unknown reference velocity, and this difference serves as a constraint in the inverse model. The ADCP velocities show good agreement with the upper ocean hydrographic velocities as indicated in Figure 6, which compares geostrophic velocities (solid line) with ADCP velocities (shaded region) along the cruise tracks.

2.4. ALACE Floats

Also included in the WOCE program were Autonomous Lagrangian Circulation Experiment (ALACE) floats which were launched roughly every 3° latitude from the hydrographic cruises used in this study and from other WOCE cruises. ALACE floats are designed to follow the current at a fixed depth (in this case about 900 m) for a predetermined period of time (here 25 days) before returning to the ocean surface and communicating their position with an Argos transmitter. They thus provide a time series of middepth velocities, averaged over a time period comparable to the eddy decorrelation scale [*Davis*, 1998].

Differences between absolute velocities from ALACE and geostrophic velocities relative to the bottom from hydrography serve as additional constraints to the inverse model. This analysis includes 504 ALACE measurements, as shown in Figure 7. A total of 4954 pairs of ALACE measurements and hydrographic stations fell within 400 km of each other.

2.5. Altimetry

The TOPEX/Poseidon satellite began returning data in mid-September 1992. Measurements of sea surface height

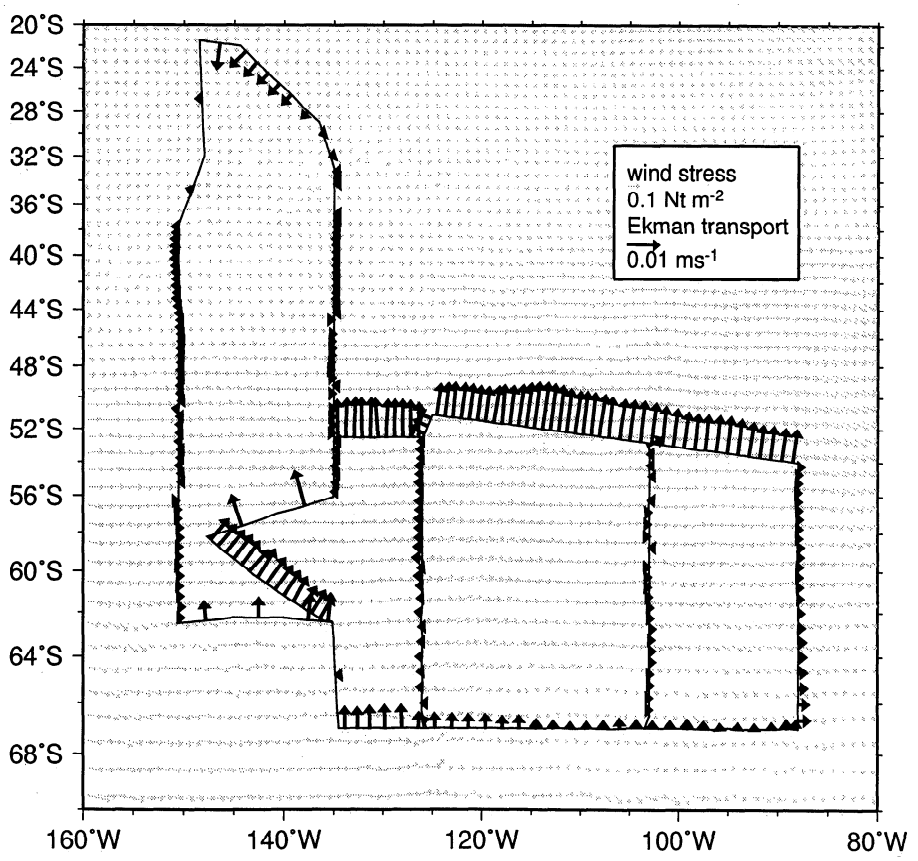

Figure 5. (Solid vectors) Cross-track Ekman velocities, assuming a 100-m-deep Ekman layer based on CERSAT wind stress estimates. Each vector represents an average for the 6-month period from September 1992 through February 1993, corresponding to the time period of the P16–P17 and P17–P19 cruises. (Shaded vectors) Mean wind stress throughout the entire region averaged over the same 6-month period.

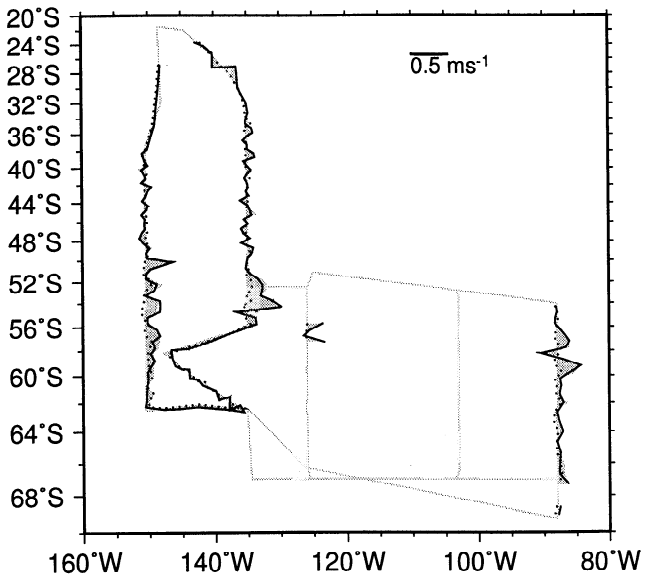

Figure 6. Near-surface velocities, perpendicular to the cruise track, averaged between 10 and 310 m depth from hydrography (solid line), and ADCP measurements (shaded region). The bottom velocities implied by the difference between ADCP and hydrographic measurements (dotted line) have a root-mean-squared value of 0.03 m s^{-1}.

variability are available every 10 days along ground tracks shown in Figure 8. For this study, only measurements from the TOPEX altimeter are used. High-frequency 10-Hz data were processed and then filtered in order to retain high wavenumber features that correspond to eddies in the Southern Ocean. All of the standard data corrections were applied, including the ocean tide, wet and dry tropospheric corrections, ionospheric correction (filtered over 50-km length scales), solid Earth tides, pole tide, an EM bias correction at high sea state, and inverse barometer correction. The time mean was removed from measured sea surface heights to produce measurements of sea surface height variability. The rms sea surface slopes were used to generate the surface eddy kinetic energy map in Figure 2.

On the basis of measured sea surface height variability, the mean sea surface height across the two primary fronts of the ACC was reconstructed using the technique outlined by *Gille* [1994]. The resulting mean sea surface height in Figure 8 indicates a total height difference of 1.2 m, roughly matching the dynamic height relative to 2500 m estimated from hydrography. Corresponding geostrophic surface velocities provide an inverse model constraint analogous to the ALACE velocities.

3. Inverse Model Results

The inverse model contained 228 constraints from the hydrography, 4954 constraints from ALACE floats, 152 constraints from ADCP measurements, and 190 constraints from altimetric sea surface height estimates, each weighted appropriately to account for the predicted measurement errors and the expected decorrelation between measurements that were not collocated in time or space. The model was set up as a matrix equation and solved using a singular value decomposition [*Wunsch*, 1996] to provide best estimates for unknown bottom velocities of 285 hydrographic station pairs as well as cross-neutral-surface velocities at the 17 interfaces in each of the four boxes. The results allow estimates of mass, heat, and salt transports through the sides of the four boxes in Figure 2.

This section will first present the results from inverse model A, which includes all the available data, as discussed in section 2. The sensitivity of these results to variations in the inverse model will be explored using models B–G.

3.1. Inverse Model A

Best estimates of the mean transport through each side of the four boxes are depicted in Figure 9, and numerical values with errors are shown in Table 2. The solution is composed of a linear combination of orthogonal vectors determined through the singular value decomposition. The challenge for the user of such a method is to decide how many singular values are dominated by physically meaningful signal rather than noise. Here the number of singular values was adjusted based on the chi-squared criterion discussed in the appendix. The calculation of formal errors shown in Tables 2, 4, and 5 is also discussed in the appendix. These error estimates represent statistical errors associated with the singular vectors included in the solution reasonably well and roughly approximate the error associated with the omitted singular vectors but may underestimate the "true" error in these solutions.

The resulting bottom velocities, shown in Figure 10, have an rms value of 8×10^{-4} m s^{-1}. Without the addition of

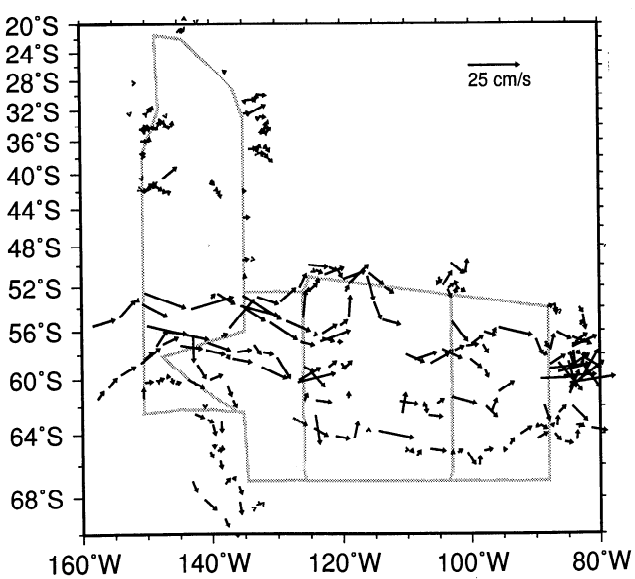

Figure 7. ALACE float velocity vectors superimposed over the cruise sampling. ALACE float vectors (in cm s^{-1}, as indicated by the scale vector) represent time averages of velocities over the 25-day interval that the floats are below the surface. The vectors are centered at the midpoint of the 25-day trajectory.

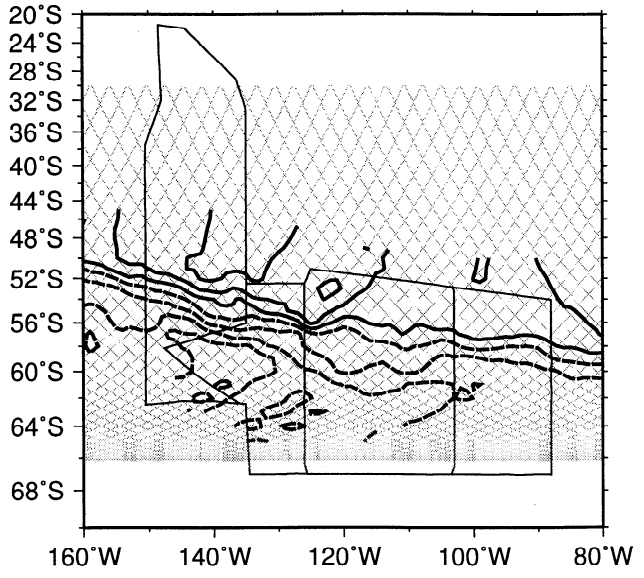

Figure 8. Mean sea surface height reconstructed from TOPEX altimeter measurements. Contour interval is 0.2 m, and negative contours (roughly corresponding to the PF) are dashed. Shaded lines indicate TOPEX ground tracks. Streamlines are closer together near 140°W, most likely because the Southern ACC Front (SF) and the subtropical gyre are near the Subantarctic Front (SAF) and the Polar Front (PF) over the East Pacific Rise.

these bottom velocities the mass transport in the four boxes would fail to balance by 41×10^9, 58×10^9, 11×10^9, and 2×10^9 kg s^{-1}, respectively. The bottom velocities reduce these imbalances to approach the a priori error of 2×10^9 kg s^{-1}. Bottom velocities tend to be largest over ridges, where the bottom is shallowest, but these high bottom velocities do not indicate high transport over topography. As the open vectors in Figure 10 indicate, the largest velocities at 2000 m depth are in deep ocean regions.

Of the 187×10^9 kg s^{-1} and 2.5 ± 0.1 PW that enter box 1 from the west, only about 105×10^9 kg s^{-1} and 1.2 ± 0.1 PW flow directly into box 2. North of box 2, 62×10^9 kg s^{-1} and 1.3 PW exit the east side of box 1, apparently as part of the subtropical gyre circulation centered in the western half of the South Pacific, as depicted by *Reid* [1986]. On the eastern side of the domain, 114×10^9 kg s^{-1} and 1.2 ± 0.1 PW flow zonally out of box 4. In contrast, *Macdonald and Wunsch* [1996] found slightly larger heat transports: in their inverse model, 1.7 PW entered the Pacific Ocean south of Australia and 1.4 ± 0.1 PW left through Drake Passage. Their elevated heat transport probably results from their constraint that the ACC carry $142\pm5\times10^6$ m^3 s^{-1}, which is larger than the zonal transport found in this model. Increasing mass transport automatically increases heat transport.

In addition to examining the total mass, salt, and heat budgets in each box, consider the transport carried by the ACC itself. For this study the northern and southern limits of the ACC are defined using a combination of criteria summarized in Table 3 in order to capture the Subantarctic Front (SAF) and the Polar Front (PF). This excludes the subtropical waters to the north and the circumpolar southern ACC front (SF) [*Orsi et al.*, 1995], which is not sampled by all of the sections. The SAF and PF are constrained to have a surface dynamic height relative to 2500 m between 1.1 and 1.95 m. On the basis of Orsi et al.'s analysis these fronts and the flow between them are expected to represent 70–80% of the total ACC transport.

Figure 11 indicates the locations of the SAF, PF, and SF based on the criteria developed by *Orsi et al.* [1995]. Range 1 of Table 4 shows the latitude range and transport of the SAF and PF selected based on these criteria. Here the latitude limits have been tuned slightly to yield a roughly constant transport through all five sections of about 100×10^9 kg s^{-1}. Range 2 of Table 4 indicates the total transport of the ACC when the three fronts are included; here, the transport is lower in sections d and e, where the SF is not fully captured by the hydrographic sections. The transport-weighted potential temperatures of the full ACC including the SF, range from 2.7 to 2.9 ± 0.1°C. These values are consistent with those of *Georgi and Toole* [1982], who found that transport weighted θ dropped from 3.1 ± 0.6 to 2.5 ± 0.3°C between New Zealand and Drake Passage and salinity constant at 34.4 ± 0.1 PSU.

Close examination of ranges 1 and 2 in Table 4 suggests that mass and heat transport vary measurably along the ACC path through the southeast Pacific. However, the transports are sensitive to small adjustments in the latitude range of the current. To evaluate whether mass and heat transport variations are real, consider the null hypothesis that SAF and PF mass, heat, and salt transport are constant in all five sections. The null hypothesis will be violated if eddy activity causes measurable changes in the ACC. Initial guesses of the lati-

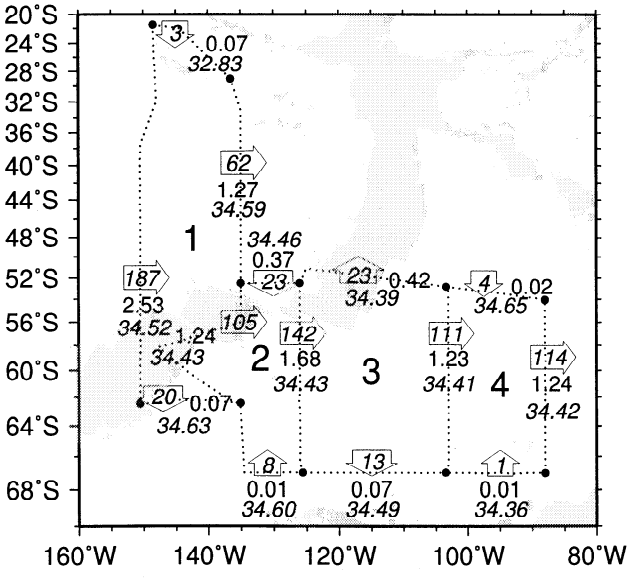

Figure 9. Best estimates of total transport, heat flux, and mean salinity transported across the sides of the four boxes used in the standard model. Mass transport estimates (in 10^9 kg s^{-1}) are enclosed in arrows to indicate the direction of flow. Heat flux (in petawatts) is in plain type, and salinities (in PSU) are in italics.

Table 2. Inverse Model Results for Each Side of the Four Boxes Identified in Figure 2.

Side	n	Mass 10^9 kg s^{-1}	Heat Flux PW	$\overline{\theta}$ °C	$\overline{S}$ PSU
			Box 1		
West	52	187 ± 8	2.53 ± 0.11	3.5 ± 0.1	34.52 ± 0.03
South	3	-20 ± 2	-0.07 ± 0.02	0.9 ± 0.2	34.63 ± 0.06
East (into box 2)	24	-105 ± 4	-1.24 ± 0.05	3.1 ± 0.1	34.43 ± 0.02
East (north of box 2)	41	-62 ± 8	-1.27 ± 0.11	5.3 ± 0.2	34.59 ± 0.07
North	7	3 ± 3	0.07 ± 0.04	7.0 ± 3.0	32.83 ± 0.70
			Box 2		
South	7	8 ± 3	0.01 ± 0.04	0.5 ± 0.8	34.60 ± 0.22
East	26	-142 ± 4	-1.68 ± 0.05	3.1 ± 0.1	34.43 ± 0.02
North	11	23 ± 4	0.37 ± 0.05	4.1 ± 0.3	34.46 ± 0.10
			Box 3		
South	13	-13 ± 4	-0.07 ± 0.05	1.4 ± 0.6	34.49 ± 0.18
East	25	-111 ± 4	-1.23 ± 0.05	2.9 ± 0.1	34.41 ± 0.02
North	28	-23 ± 7	-0.42 ± 0.09	4.7 ± 0.5	34.39 ± 0.16
			Box 4		
South	10	1 ± 3	0.01 ± 0.04	1.8 ± 7.7	34.36 ± 2.39
East	24	-114 ± 6	-1.24 ± 0.07	2.8 ± 0.1	34.42 ± 0.03
North	13	4 ± 4	0.02 ± 0.06	1.0 ± 1.7	34.65 ± 0.57

The value n indicates the number of station pairs defining each side of the boxes. Mass transport, heat flux, and the effective mean potential temperature and mean salinity of the transported water are indicated along with error estimates. Positive transports and heat fluxes correspond to mass and heat entering the box. Formal errors provide a rough estimate of one standard deviation uncertainties in these estimates but cannot account for all of the null space in the SVD [*Wunsch*, 1996].

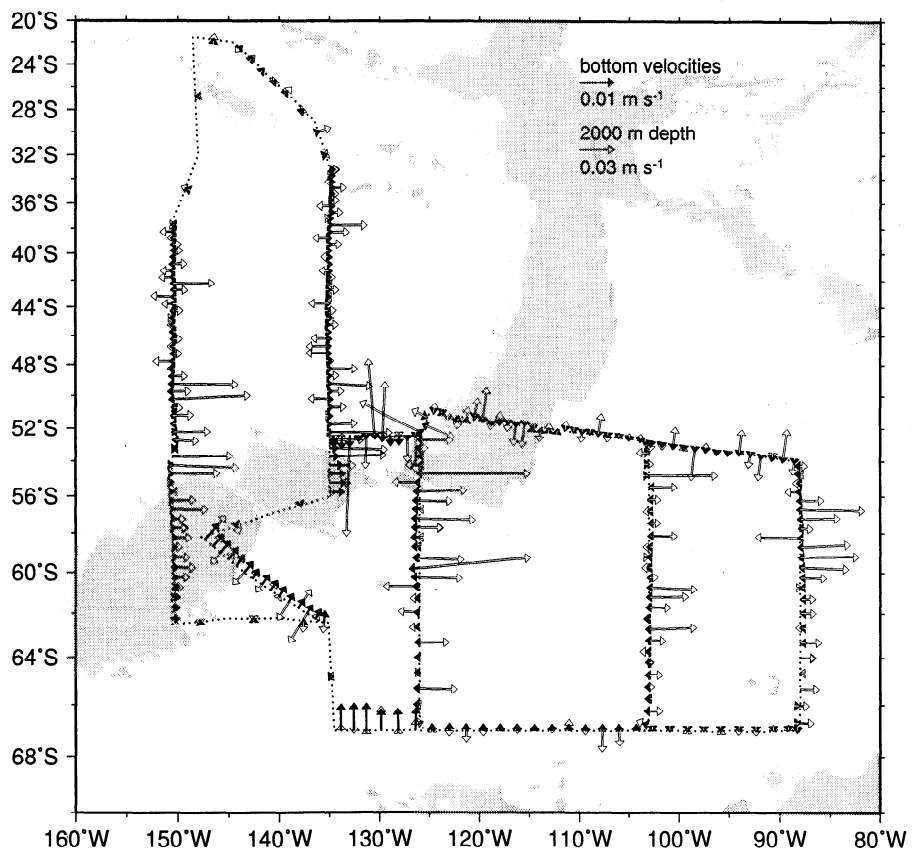

Figure 10. (Solid arrows) Best estimates of bottom velocities across the sides of the four boxes and (open arrows) corresponding velocities at 2000 m depth. Shaded regions delineate depths shallower than 3500 m.

Table 3. Potential Temperature and Salinity Indicators for the Major ACC Fronts Used in This Study.

Front	Indicators
SAF	$S < 34.20$ at $Z < 300$ m to the south
	$\theta >$ 4-5°C at 400 m to the north
PF	$\theta < 2$°C along θ-min at $Z <$200 m to the south
	$\theta > 2.2$°C along θ-max at $Z >$400 m to the north
SF	$\theta < 0$°C along θ-min at $Z <$150 m to the south
	$S > 34.73$ along S-max at $Z >$ 800 m to the north

From *Orsi et al.* [1995].

tude limits defining the SAF and PF in the five sections are tuned by minimizing the objective function:

$$J = \sum_{i=1}^{5} \left[\left(\frac{M_i - \overline{M}}{\sigma_M} \right)^2 + \left(\frac{h_i - \overline{h}}{\sigma_h} \right)^2 + \left(\frac{s_i - \overline{s}}{\sigma_s} \right)^2 \right] \quad (2)$$

where M is mass transport, h is heat transport, s is salt transport, overbars represent means over the five sections, and σ is the mean statistical error for each of these quantities. The sizes of M_i, h_i, and s_i are adjusted by varying the latitudes of the northern and southern limits of the SAF plus PF.

Figure 12 depicts the transport carried by the SAF and PF, defined by minimizing J, and range 3 of Table 4 provides detailed transport information with errors. The large-scale trend through the study region shows little change in the heat or salt transport of the ACC through the five sections. Thus, despite the intense eddy activity associated with the Eltanin–Udintsev Fracture Zone, the ACC's properties do not change sufficiently to distinguish the current from the null hypothesis which presumes that the ACC is a barrier to mixing that does not interact with its surroundings in the southeastern Pacific Ocean.

3.2. Variations to the Inverse Model

The errors in Table 4 indicate the formal statistical error of the results, but they do not account for possible problems in the assumptions underlying the inverse model. This section explores the sensitivity of the results to the inverse model design. In each case, results shown represent the SAF and PF transports once the objective function J defined in (2) has been minimized. Since the objective function J was minimized separately for each of these variant inverse models, the latitude range and mean transport differ slightly in each case, and each can be considered an independent estimate of transport variations in the ACC.

In their earlier study, *Georgi and Toole* [1982] assumed that the bottom velocities in the Southern Ocean were zero, instead of running an inverse model. In Table 5, model B has bottom velocities and interfacial velocities defined to be zero, with the bottom velocity error assumed to be 0.02 m s^{-1}. The model B results, indicated in Table 5, are not statistically different from the inverse model A. Thus the initial guess that the bottom velocities are zero differs little from the mass-balanced inverse solution.

Many inverse models are limited to hydrographic data. To test whether the direct-velocity measurements from the ADCP, ALACE floats, and altimetry influenced the model output, the inversion was rerun using only the hydrographic data. Model C in Table 5 indicates the best results for ACC transport. Although the latitude ranges selected are slightly different, the transports and fluxes are nearly identical to model A. This suggests that the ancillary measurements have done little to alter the inverse solution or the apparent large-scale circulation. This finding is consistent with those of other inverse models that have incorporated direct-velocity measurements [*Joyce et al.*, 1986; *Bingham and Talley*, 1991; *Mercier et al.*, 1993]. In the Kuroshio, *Bingham and Talley* [1991] found that using direct velocity measurements to determine the initial reference velocity guesses reduced the a priori mass imbalance. However, for the Southern Ocean example, this was not the case, and only solutions with an initial guess of zero bottom velocity were considered.

Although direct-velocity measurements do not significantly alter the solution, they do change the structure of the singular values. Singular values based on hydrography alone (solid line in Figure 13) drop off rapidly with increasing singular mode number. Since the hydrography provides redundant information for the large-scale budgets in the inverse model boxes, higher-order modes provide progressively less new information. In contrast, the inverse model treats direct-velocity measurements as spatially uncorrelated information, and the corresponding singular values are nearly constant with increasing singular mode (dashed line in Figure 13). For the cases examined here, the a priori errors of the direct-velocity measurements are so large that the direct velocities do not have a significant impact on the final solution. These solutions depend primarily on the hy-

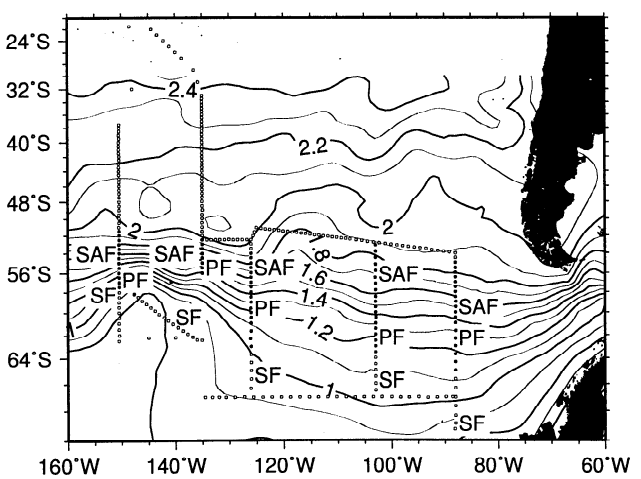

Figure 11. Dynamic height (in m) at the surface relative to 2500 m depth, from the *Olbers et al.* [1992] gridded atlas data, which covers the region south of 30°S. Hydrographic stations with dynamic height values between 0.9 and 2.0 (solid dots) define the ACC, and the locations of the SAF, PF, and SF are indicated, based on the criteria of *Orsi et al.* [1995].

Table 4. Inverse Model A Results for the Transports Carried by the ACC Through the Five Meridional Sections Identified in Figure 12.

Section	n	Range	Mass, 10^9 kg s^{-1}	Heat Flux, PW	$\overline{\theta}$, °C	$\overline{S}$, PSU
		Range 1: SAF and PF From Water Mass Signatures				
a	12	51.0°–57.0°	98 ± 4	1.20 ± 0.05	3.1 ± 0.1	34.41 ± 0.02
b	9	52.0°–57.0°	110 ± 3	1.50 ± 0.03	3.5 ± 0.1	34.42 ± 0.01
c	16	54.5°–63.0°	102 ± 3	1.30 ± 0.04	3.3 ± 0.1	34.41 ± 0.02
d	19	53.8°–64.5°	106 ± 3	1.26 ± 0.04	3.1 ± 0.1	34.40 ± 0.02
e	15	56.0°–64.3°	107 ± 4	1.24 ± 0.06	3.0 ± 0.1	34.42 ± 0.02
		Range 2: SAF, PF and SF From Water Mass Signatures				
a	17	51.0°–59.5°	126 ± 5	1.33 ± 0.06	2.7 ± 0.1	34.44 ± 0.02
b	11	52.5°–58.2°	113 ± 3	1.28 ± 0.03	2.9 ± 0.1	34.44 ± 0.01
c	21	54.5°–66.3°	125 ± 4	1.42 ± 0.05	2.9 ± 0.1	34.43 ± 0.02
d	26	52.8°–67.0°	111 ± 4	1.23 ± 0.05	2.9 ± 0.1	34.41 ± 0.02
e	20	55.5°–67.0°	118 ± 5	1.28 ± 0.06	2.8 ± 0.1	34.42 ± 0.03
		Range 3: SAF and PF After Minimizing Transport, Salt, and Heat Variations				
a	12	51.5°–57.5°	101 ± 4	1.21 ± 0.05	3.1 ± 0.1	34.41 ± 0.02
b	9	52.5°–58.2°	104 ± 2	1.25 ± 0.03	3.1 ± 0.1	34.42 ± 0.01
c	17	54.0°–63.0°	100 ± 3	1.26 ± 0.04	3.2 ± 0.1	34.41 ± 0.02
d	19	52.8°–63.5°	102 ± 4	1.17 ± 0.04	3.0 ± 0.1	34.41 ± 0.02
e	19	54.5°–65.0°	102 ± 5	1.17 ± 0.06	3.0 ± 0.1	34.41 ± 0.03

Three separate ACC ranges are considered. The first is based on *Orsi et al.*'s [1995] potential temperature and salinity constraints, slightly adjusted so that the PF and SAF roughly conserve transport. The second uses potential temperature and salinity signatures that encompass the SF, PF, and SAF. The third tests the null hypothesis that the total transport of the PF and SAF does not vary, by minimizing an objective function that forces conservation of heat and transport. The value n indicates the number of station pairs assumed to be within the ACC. Mass transport, heat flux, and the effective mean potential temperature and mean salinity of the transported water are indicated along with error estimates. Positive transports and heat fluxes are eastward.

drographic measurements that dominate the first 59 singular values. Tests based on varying row weightings indicate that that the direct-velocity measurements would more strongly influence the solutions if they were at least 5 times more numerous or (roughly equivalently) if the direct-velocity errors were a factor of $\sqrt{5}$ smaller.

This sensitivity to direct-velocity errors might seem to indicate that merely by decreasing the size of the a priori error bars, one could force the direct velocities to control the inverse solution. This is not the case, since solutions with smaller a priori errors would violated the chi-square criterium discussed in the appendix. The results of model A were achieved by perturbing initial error estimates by only a small amount in order to insure that the chi-square condition was met. Further exploration of parameter space did not yield any consistent balance in which direct-velocity measurements more strongly influenced the solution, apparently because direct velocities are highly variable and not generally consistent with hydrography.

The wind stresses over the Southern Ocean are among the largest in the world, but the actual Ekman transports induced by the winds are estimated to be small compared with the geostrophic transports. Since the wind measurements from the scatterometer are noisy and imperfect, and the Ekman transports appear small, model D omitted wind forcing. The results listed in Table 5 were not significantly different from the results found with wind forcing.

This model allowed for some advection of mass, heat, and salt across neutral surfaces. If properties were exactly conserved on neutral surfaces, cross-neutral surface transfer would be zero. Thus model E suppressed interlayer transfer. As shown in Table 5, ACC properties were again nearly

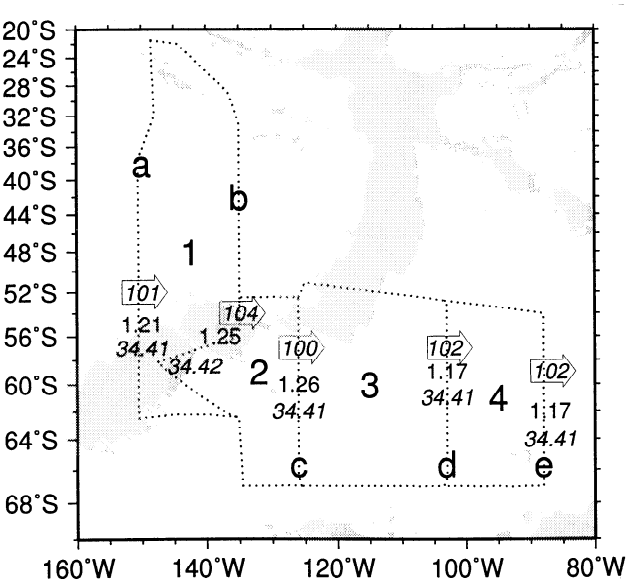

Figure 12. Best estimates of mass, heat, and salinity transported by the SAF and PF of the ACC across the five meridional sections. Transport estimates (in 10^9 kg s^{-1}) are enclosed in arrows to indicate the direction of flow. Heat transport (in PW) is in plain type, and salinities (in PSU) are in italics.

Table 5. Model Results for the Variations Described in the Text, Indicating Transports Carried by the ACC Through the Five Meridional Sections Identified in Figure 9.

Section	n	Range	Mass, 10^9 kg s^{-1}	Heat Flux, PW	$\overline{\theta}$, °C	$\overline{S}$, PSU
			Model B (Zero Reference)			
a	13	51.5°–58.0°	107 ± 8	1.24 ± 0.11	3.0 ± 0.1	34.41 ± 0.05
b	9	52.5°–58.2°	96 ± 25	1.22 ± 0.33	3.2 ± 0.5	34.41 ± 0.17
c	19	53.0°–63.0°	105 ± 12	1.22 ± 0.16	3.0 ± 0.2	34.44 ± 0.07
d	21	52.8°–64.5°	103 ± 14	1.18 ± 0.19	2.9 ± 0.2	34.41 ± 0.08
e	18	55.0°–65.0°	105 ± 14	1.19 ± 0.19	2.9 ± 0.2	34.42 ± 0.08
			Model C (Hydrography Only)			
a	13	51.0°–57.5°	102 ± 4	1.22 ± 0.05	3.1 ± 0.1	34.41 ± 0.02
b	9	52.5°–58.2°	106 ± 2	1.26 ± 0.03	3.1 ± 0.1	34.43 ± 0.01
c	16	54.5°–63.0°	102 ± 3	1.29 ± 0.04	3.3 ± 0.1	34.41 ± 0.02
d	21	53.2°–65.0°	104 ± 4	1.19 ± 0.05	3.0 ± 0.1	34.41 ± 0.02
e	16	55.5°–64.3°	104 ± 4	1.20 ± 0.06	3.0 ± 0.1	34.41 ± 0.03
			Model D (No Wind)			
a	13	51.5°–58.0°	106 ± 4	1.23 ± 0.05	3.0 ± 0.1	34.41 ± 0.02
b	9	52.5°–58.2°	106 ± 2	1.27 ± 0.03	3.1 ± 0.1	34.42 ± 0.01
c	15	54.5°–62.3°	108 ± 4	1.33 ± 0.04	3.2 ± 0.1	34.42 ± 0.02
d	23	53.8°–64.5°	105 ± 4	1.25 ± 0.05	3.1 ± 0.1	34.40 ± 0.02
e	15	56.0°–64.3°	106 ± 4	1.23 ± 0.06	3.0 ± 0.1	34.41 ± 0.03
			Model E (No Vertical Velocities)			
a	12	51.5°–57.5°	103± 4	1.22 ± 0.05	3.1 ± 0.1	34.41 ± 0.02
b	8	52.5°–57.0°	96 ± 2	1.20 ± 0.03	3.2 ± 0.1	34.42 ± 0.01
c	16	54.0°–62.3°	100 ± 4	1.26 ± 0.04	3.2 ± 0.1	34.41 ± 0.02
d	21	52.8°–64.5°	100 ± 4	1.16 ± 0.05	3.0 ± 0.1	34.41 ± 0.02
e	18	54.5°–64.3°	102 ± 5	1.17 ± 0.06	3.0 ± 0.1	34.41 ± 0.03
			Model F (Three Boxes)			
a	12	51.5°–57.5°	97 ± 4	1.19 ± 0.05	3.1 ± 0.1	34.41 ± 0.02
b	9	52.5°–58.2°	100 ± 2	1.23 ± 0.03	3.1 ± 0.1	34.45 ± 0.01
c	17	54.0 °–63.0°	99 ± 3	1.33 ± 0.05	3.3 ± 0.1	34.37 ± 0.02
e	16	55.0°–64.3°	99 ± 5	1.22 ± 0.06	3.1 ± 0.1	34.37 ± 0.03
			Model G (No Heat Constraints)			
a	12	52.0°–58.0°	103 ± 4	1.19 ± 0.05	3.0 ± 0.1	34.41 ± 0.02
b	9	52.5°–58.2°	104 ± 2	1.27 ± 0.03	3.1 ± 0.1	34.42 ± 0.01
c	16	54.0°–62.3°	105 ± 3	1.28 ± 0.04	3.2 ± 0.1	34.42 ± 0.02
d	22	52.8°–65.0°	105 ± 4	1.19 ± 0.05	2.9 ± 0.1	34.41 ± 0.02
e	17	55.5°–65.0°	104 ± 5	1.20 ± 0.06	3.0 ± 0.1	34.42 ± 0.03

Values shown are as in Table 3, and the model cases are discussed in the text.

constant through all sections and scarcely differed from the previous estimates. (However, based on tests with numerical model output, *McIntosh and Rintoul* [1997] noted that better results are expected when diapycnal fluxes are incorporated into the inversion model, and they suggested using separate fluxes for mass, heat, and salt.)

Since the ACC may vary substantially from one year to the next, model F considers a reduced three-box model for which all of the hydrographic data is drawn from a 4-month period in 1992. In this model, boxes 3 and 4 are merged into a single box, and the southern sides of the middle and eastern boxes are closed by computing the large-scale geostrophic transport between the southernmost stations on the meridional sections as indicated with a dotted line in Figure 2. The model uses 234 hydrographic station pairs, compared with 285 in the full inverse model, and includes the same ancillary measurements from ALACE floats, ADCP measurements, and altimetry. Within errors, the resulting SAF and PF mass and heat transports in Table 5 are nearly the same for model F as they are for model A. Section c appears slightly warmer, and sections c and e are slightly fresher than in model A. Given the uncertainties associated with the sparse station sampling, these differences are not significant enough to demonstrate a substantial difference between the full inverse model and the reduced single-season inverse model.

Finally, since heat transport processes are a prime interest, model G suppresses the heat budget constraints imposed by the hydrographic data. The results are indistinguishable from model A results, suggesting that the interpretation of the heat budget is not biased by imposing heat constraints in the analysis. Since model G does not force the oceanic heat budgets in each box to close, box 1 loses 0.05 ± 0.17 PW to the atmosphere, box 2 loses 0.07 ± 0.10 PW, box 3 loses 0.01 ± 0.13 PW, and box 4 gains 0.02 ± 0.12 PW. These heat imbalances are not significantly different from zero, suggesting that regional air-sea heat exchanges are not large enough to be detectable in this inverse model budget.

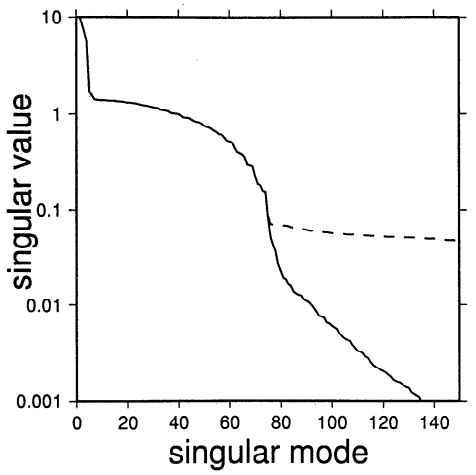

Figure 13. Magnitude of singular values as a function of singular mode number for model C corresponding to the inversion of hydrography only (solid line) and for model A corresponding to the full inversion (dashed line). The dashed and solid lines coincide up to about singular mode 75.

Trends in heat transport, $\overline{\theta}$ and $\overline{S}$ for models B to G all agree with those from model A within errors in Table 5. In addition, the model transports through all sides of the boxes are nearly the same in each of the inverse models considered. Therefore model A results will be treated as a robust solution in the discussion that follows.

4. Discussion

4.1. Heat Transfer

The variations in SAF and PF heat transport summarized in range 3 of Table 4 imply that in each box, the ACC's heat flux divergence is at most 0.11 PW. As noted earlier, these results are indistinguishable from the null hypothesis that the ACC does not exchange heat or salt with surrounding subtropical and subpolar waters. How do the ACC heat transport estimates generated by this inverse model then compare with other heat flux estimates? Table 6 summarizes meridional heat transfer estimates from a suite of previous studies of the south Pacific and of the global ocean. Most of these studies indicate relatively small total heat fluxes. For example, *Macdonald and Wunsch* [1996] found an northward heat transfer of 0.3 ± 0.3 PW in the Pacific sector of the Southern Ocean. If a meridional heat transport of this magnitude were distributed evenly across the Pacific Ocean, the heat transport out of any given 20° wide segment would be difficult to detect. In contrast, if meridional heat transfer were concentrated in a few narrow segments of ocean, some boxes might show measurable heat flux.

The eddy-induced diffusivity parameterization suggested by *Keffer and Holloway* [1988] implies highly inhomogeneous southward heat fluxes that are correlated both with eddy activity and local mean temperature gradients, both of which vary across the southeastern Pacific. The large-scale mean circulations depicted by *Reid* [1986] and the dynamic height map (Figure 11) both indicate that as the ACC crosses over the East Pacific Rise, contours of geopotential anomaly pinch together bringing recirculating subtropical waters in close contact with the circumpolar SAF and PF, just about at the location where EKE is greatest. The formulation of *Keffer and Holloway* [1988], though sensitive to choice of scaling factors, predicts southward flux across 53°S of 0.19 PW into box 1, 0.07 PW into box 2, 0.05 PW into box 3, and 0.02 PW into box 4. Southward heat fluxes across 64°S are expected to be smaller, at 0.00 PW, 0.01 PW, 0.03 PW, and

Table 6. Selected Northward Meridional Heat Fluxes Estimated in Previous Studies of the South Pacific and Complete Southern Ocean.

Latitude	Pacific[a]	Global[a]	Reference	Method
30°S	0.09±0.26	-0.51	*Sloyan* [1997]	ocean inverse model
40°S	-0.09 to 0.04	-0.66	*Georgi and Toole* [1982]	analysis of meridional sections (with air-sea exchange)
	-2.2	-2.2	*Talley* [1984]	surface heat budgets
	0.09	-0.90	*Hsiung* [1985]	mean surface energy fluxes integrated from north south
27°–43°S		-0.5 ± 0.30	*Macdonald and Wunsch* [1996]	ocean inverse model
43°S	-0.15 to 0.42		*Bennett* [1978]	analysis of zonal hydrographic sections
43°S	-0.10 to 0.13 ±0.11		*Wunsch et al.* [1983]	inverse model of zonal hydrographic sections
	0.3 ± 0.3		*Macdonald and Wunsch* [1996]	ocean inverse model
53°S		-0.70	*Keffer and Holloway* [1988]	altimeter data plus turbulence closure
South of ACC		-0.31	*Gordon and Owens* [1987]	global ocean heat balance
60°S	-1.19	-0.19	*Hastenrath* [1980]	mean surface energy fluxes integrated from north to south
60°S		-0.54	*Gordon* [1981]	air-sea heat exchange integrated between 60° and 70°S
60°S		-0.65	*Hastenrath* [1982]	mean surface energy fluxes integrated from north to south

[a]Heat fluxes in 10^{15} W (= PW).

0.02 PW. The large southward heat flux into box 1 is due to the eddy peak at 53°S, while heat flux out the southside of box 1 may be blocked by the East Pacific Rise. The resulting 0.2 PW net flux into box 1 is sufficient to suggest that the heat transport of the ACC should rise measurably in box 1. No such large variation in heat transport is observed in this inverse model, in box 1 or elsewhere, nor does the heat transport of the ACC monotonically increase as it flows westward, as this schematic eddy-induced heat transport would require. ACC heat transport is effectively constant. Heat that enters the model domain in box 2 flows northward out of box 3, and there is no evidence that sections d and e are measurably warmer than section a. Therefore heat transport into the ACC does not appear intensified by high EKE, possibly because much eddy mixing transfers water primarily along neutral-density surfaces without influencing the net heat budget. If heat enters the ACC through strong southward eddy mixing, it must leave as quickly through vertical exchanges with the atmosphere and meridional exchanges with the surrounding ocean.

A simpler view of subtropical to Southern Ocean heat exchange assumes that heat fluxes are relatively constant along the length of the ACC. On the basis of Southern Ocean hydrographic data, *deSzoeke and Levine* [1981] estimated the mean eddy heat transport across the ACC to be 5.6×10^3 W m^{-2}. From current meter measurements in Drake Passage, *Johnson and Bryden* [1989] estimated slightly larger eddy-induced meridional heat fluxes, ranging from 8×10^3 W m^{-2} below about 2500 m depth up to 16×10^5 W m^{-2} at the upper most instruments at 580 m depth. For a 4000-m-deep ocean these values would allow a southward meridional heat transport of about 0.05 PW in box 1, about 0.03 PW in box 2, 0.07 PW in box 3, and 0.05 PW in box 4. These values are about the same magnitude as the negligibly small changes in ACC heat transport implied by the inverse model. Taken together, however, they would imply a net heat transport increase between sections a and e of 0.2 PW, which is not justified by this inverse model.

Heat transfer within the ocean must also balance exchanges with the atmosphere. Air-sea heat flux rates in the Southern Ocean are not well known: *Hsiung* [1985] indicated that the Southern Ocean loses heat to the atmosphere but identified no data in the southeastern Pacific. On the basis of ECMWF analyses, *Barnier et al.* [1995] estimated the heat loss from the ocean to the atmosphere in the southeastern Pacific to vary from 20 to 110 W m^{-2}. Assuming that the ACC is roughly 5° wide, then the maximum Barnier heat loss of 110 W m^{-2} would suggest that the ACC should lose roughly 0.04 PW between sections a and b, 0.06 PW between sections b and c, and 0.10 PW between sections c and d, and 0.06 PW between sections d and e. These fluxes are of the right sign and magnitude to balance the small meridional heat transport into this region and are consistent with the small variations in ACC heat transport found by the inverse model.

Although the ACC passes through highly variable environments as it traverses the southeastern Pacific, it appears to gain and lose heat only in small quantities that might be predicted from basin-scale averages. Therefore most of the heat exchange in the ACC probably occurs elsewhere in the ocean, most likely in the Indian Ocean as global investigations have suggested [*Georgi and Toole*, 1982; *Macdonald and Wunsch*, 1996; *Sloyan*, 1997]. The small changes in ACC heat content in each of this inverse model's four boxes in the southeastern Pacific appear well within the ranges suggested either by basin-scale eddy heat flux estimates or by air-sea exchange rates.

4.2. Layer-by-Layer Transport

Figure 14 shows the SAF and PF transport as a function of neutral-density layer through each of the five sections. The vertical structure of mass transport varies little as the ACC flows eastward, although sections d and e show some transport in the upper four layers, implying a slight change in the upper ocean properties of the SAF. Overall, transport is concentrated between layers 5 and 16 with maxima between layers 6 and 7 and between layers 14 and 15. The shallower maximum is concentrated in intermediate water and is predominantly contained in the upper 1000 meters within the SAF. The transport maximum in layers 14 and 15 represents a thick layer of deep water that is concentrated between 2000

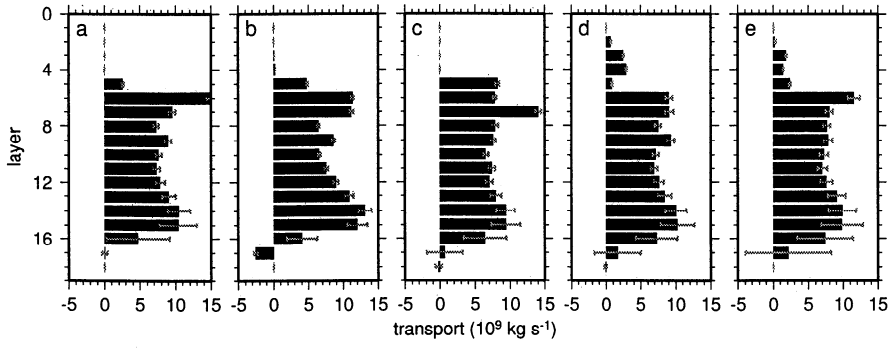

Figure 14. Best estimates of SAF and PF eastward transport (in 10^9 kg s^{-1}) as a function of neutral-density layer for each of the five sections identified in figure 12. The latitude range used to define the SAF and PF is the same as range 3 of Table 4. Shaded bars indicate magnitude of estimated transport error. Within the model domain, layers 1 to 12 outcrop.

and 3000 m depth in the SAF and between 1000 and 2000 m depth in the PF. This deep layer maximum is stronger in the PF, because its water masses are shallower and therefore faster moving.

Layer-by-layer heat transport, shown in Figure 15 is concentrated in the same layers as mass transport. Unlike mass transport, heat transport does not have a strong secondary maximum at layers 14 and 15 but is concentrated between layers 5 and 7. These upper ocean layers outcrop and do not include water south of the SAF. Therefore these results indicate that most of the ACC heat transport is concentrated in intermediate water layers in the upper 1000 meters of the SAF.

Schematics of the Southern Ocean suggest that the meridional circulation should be dominated by northward Ekman transport which returns via a southward geostrophic flow at depths below the sill depth where topographic features are able to establish a net pressure gradient [e.g., *Johnson and Bryden*, 1989; *Warren*, 1990; *Döös and Webb*, 1994]. Upwelling is imagined to happen along isopycnals, in the core of the ACC where the wind stress is strongest and where most of the layers outcrop. Figure 16 shows the mass and heat transports through the northern and southern sides of the boxes by water mass category. On the north side, mass and heat that flow into box 2 flow out of box 3, and total transports are not always distinguishable from noise. The net transport through the northern sides of boxes 2, 3, and 4 is nonetheless consistent with the schematic overturning, with small northward mass and heat flow in the intermediate water mass layers and southward flow in the deep water mass layers. Extrapolating these results to the global ocean implies a lower limit on the meridional overturning cell of 20 to 55 $\times$ 10^9 kg s^{-1} and 0.3 to 0.5 PW at 52°S. The northern side of box 1 is far north of the ACC and should have little relation to Southern Ocean processes.

On the south side of the ACC, little intermediate water is present (see Figure 16), and the inverse model indicates only weak overturning circulation with southward flow of surface intermediate waters and some northward flow of deep and bottom waters particularly in boxes 2 and 4. Since the overturning appears weaker in the south than in the north, most of the upwelling associated with the overturning cell should be contained in the latitude range of the ACC. In box 3, significant southward flow of deep water is probably due to the SF flowing out of the model domain. In box 1, southward flow of deep water may be part of a deep western boundary current along the eastern flank of the East Pacific Rise. As part of the WOCE chemical sampling program, chlorofluorocarbon (CFC) measurements were also collected on these research cruises. Because CFCs are anthropogenic, only water that has recently been in contact with the atmosphere should have measurable amounts of CFC. Along the southern side of box 1, high CFC concentrations suggest that recently ventilated water flows northward along the eastern flank of the East Pacific Rise as bottom water, as the bottom velocities in Figure 10 indicate. Close examination of the layer-by-layer inverse model results suggests the presence of two separate deep western boundary currents in box 1 (not illustrated). In layer 18, 0.2 $\times$ 10^9 kg s^{-1} of bottom water flows northward through the southside of box 1, but southward flow in layer 17 overwhelms the net bottom water budget.

4.3. Water mass Conversion

Diapycnal fluxes of mass, heat, and salt in the inverse model provide a diagnostic to indicate where water mass formation processes occur. Regions in which diapycnal mass, heat, and salt transfer are large are places where water masses are not completely conserved on neutral surfaces. Figure 17 indicates diapycnal mass, heat, and salt divergences as a function of model layer for the four boxes. Error bars are not shown but are generally of the same order of magnitude as the flux divergences themselves, as is expected since the flux divergences are by definition constrained to be small deviations about zero that should lie within predicted error bars. (Although these diapycnal fluxes are computed using the same vertical velocities for each of the three properties, they are similar in magnitude and sign to flux divergences obtained by allowing the inverse model to establish separate diapycnal advection rates for mass, heat, and salt, as *Sloyan* [1997] did. The matrices that must be inverted in order to compute separate diapycnal fluxes are much larger than the matrices required for simple diapycnal fluxes that use the same advection rates for all three quanti-

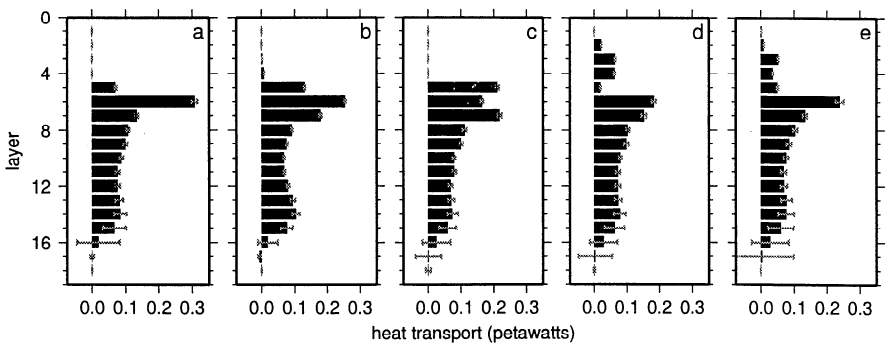

Figure 15. Solid bars indicate best estimates of ACC heat transport (in petawatts = 10^{15} W) as a function of neutral-density layer for each of the five sections identified in Figure 12. Shaded bars indicate magnitude of estimated errors.

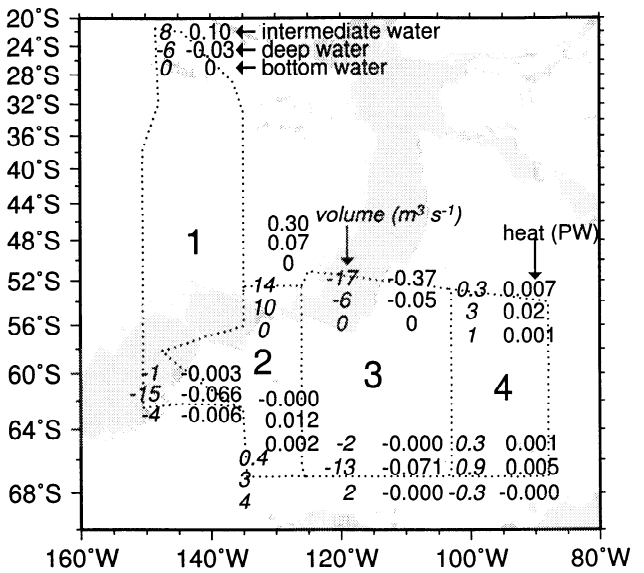

Figure 16. Circulation through the northern and southern boundaries of the inverse model as a function of layer depth. Italicized numbers indicate mass transport in 10^9 kg s^{-1} and plain text indicates heat transport in petawatts. Stacks of numbers show intermediate water (layers 1 to 10) on top, deep water (layers 11 to 16) in the middle, and bottom water (layers 17 and 18) on the bottom. On both the southern and northern boundaries, positive values indicate transport into the model domain.

ties. These large matrix inversions were judged too computationally burdensome for this study.)

The flux divergences vary substantially in sign, indicating that some layers gain mass, heat, or salt, while adjacent layers lose the same properties. Similarly, the diapycnal velocities (not shown) change sign rapidly in the vertical, indicating that properties are not systematically transported in one direction, either upward or downward, as would be expected if there were constant mid-ocean diffusion.

Flux divergences are largest in the outcropping layers near the surface and in the deepest layers of the model with low flux divergences in the deep water layers of the model. The large magnitude of upper ocean heat flux divergences suggests that the processes associated with air-sea heat and freshwater exchange and the associated meridional overturning cell play a much larger role in diapycnal water mass transfer than do any processes that occur in the deep ocean. In the ocean these layers outcrop just to the north of and within the SAF. Air-sea heat and freshwater exchanges in these locations particularly play a role in Subantarctic mode water formation [*McCartney*, 1977].

High diapycnal fluxes within deep layers of the ocean in Figure 17 may result from insufficient sampling of dense water input along the southern boundary of the model, but these high bottom water fluxes may also indicate that diapycnal mixing rates increase near the bottom of the ocean, as microstructure measurements clearly indicate [*Polzin et al.*, 1997]. Bottom mixing appears largest in box 2, which is a small box dominated by large bathymetric features, suggesting that greater diapycnal mixing may occur when flow passes over bathymetry.

5. Summary

This study has used an inverse model to combine hydrographic measurements taken in the southeastern Pacific between January 1992 and March 1994 with ADCP velocities, ALACE float velocities, TOPEX altimeter surface geostrophic velocities, and ERS scatterometer wind forcing. As in previous inverse modeling studies, the constraints imposed by direct measurements did not significantly alter the results of the inverse model based on hydrography alone.

The inverse model was used to examine mass, heat, and salt transfer through the southeastern Pacific. The results were examined to see whether eddy activity in the southeastern Pacific Ocean carries heat southward from the subtropical gyre to warm up the main fronts of the ACC: the SAF and the PF. This study found that the ACC is little changed as it passes through the region of high eddy activity located on top of and downstream from the East Pacific Rise. Although warm subtropical water is in close proximity to the ACC fronts as they cross over the mid-Pacific Ridge and high eddy activity could mix these water masses together, the actual exchange of water appears to be negligibly small. The jets associated with the SAF and PF are estimated to transport about 102×10^9 kg s^{-1}, and 1.2 PW, with a mean salinity of 34.41 PSU. Individual sections deviate only slightly from these mean values.

Mass transfer as a function of neutral density has maxima in two separate density classes, one in intermediate water associated with the SAF and the second in denser deep water more closely associated with the PF. Heat transport is associated with the mass transport peak in the SAF, in the northern half of the ACC. On the northern edge of the inverse model domain, meridional circulation is consistent with an overturning stream function that carries intermediate water northward and returns deep water southward. On the southern boundary of the domain, deep and bottom waters flow both northward and southward but are generally consistent with a weaker overturning circulation. Finally, the Southern Ocean is a region of large air-sea interaction, and diapycnal

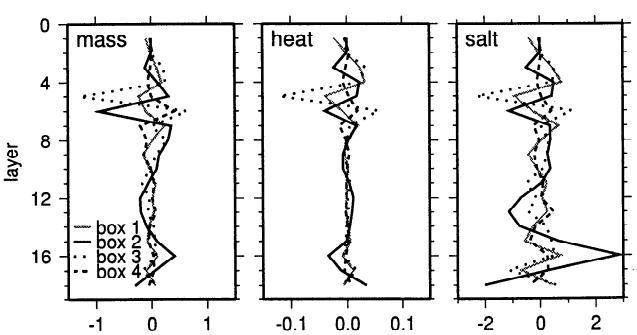

Figure 17. Diapycnal flux divergences of mass (10^{10} kg s^{-1}), heat (PW), and salt (PSU $\times 10^6$ m^3 s^{-1}). As in the other inverse model results, positive flux divergences indicate net input to a layer.

fluxes in the inverse model indicate that water mass transformation occurs predominantly in outcropping upper layers of the ocean. Specific details of heat exchanges between the ACC and the subtropics and between the ocean and atmosphere are too small to detect within model error bars. Together the model results suggest that despite variations in topography and eddy activity, the large-scale structure of the ACC is relatively constant in the southeastern Pacific.

Appendix: Inverse Model and Weights

A1. Inverse Model Equations

The inverse model is designed to find reference velocities in order to adjust thermal wind velocities from hydrographic data to conserve mass, heat, and salt within each of the boxes and on each of the layers of the model. The basic equations have been discussed extensively [*Rintoul*, 1991; *Macdonald*, 1993; *Macdonald and Wunsch*, 1996; *Wunsch*, 1996] and are presented briefly here. For each layer and in each box the equations representing the conservation of mass, heat, or salt can be written

$$\sum_{i=1}^{N} \theta_i l_i h_i (v_i + b_i) - w_t \theta_t a_t + w_b \theta_b a_b = -E(\theta_i) \quad \text{(A1)}$$

where i is the station pair number, and there are a total of $N = 285$ station pairs. The variable θ can be density, potential temperature anomaly, or salinity anomaly, l is the distance between the two stations, h is the height of the neutral density layer, v is the geostrophic velocity into the box relative to the reference level depth, b_i is the unknown velocity at the reference level (here defined to be the deepest common depth for each station pair), w_t is the vertical velocity out of the top of the box, w_b is the vertical velocity into the bottom of the box, a_t and a_b represent the horizontal areas enclosed by the box at its top and bottom, and $E(\theta_i)$ is the surface Ekman transport for layers that outcrop and zero otherwise. Potential temperature and salinity budgets are dominated by the mass budget. In order to force the mass, temperature, and salt constraints to contribute independent information, mean values of θ and S are removed and the anomaly fields are used. Geostrophic velocities below the deepest common depth are estimated by extrapolating dynamic height anomalies below the bottom of the shallower CTD cast using a second-order polynomial fit.

The constraints represented in (A1) may be written as a matrix equation of the form

$$\mathbf{A}\mathbf{b} = \mathbf{T}, \quad \text{(A2)}$$

where the matrix $\mathbf{A}$ in this case has 216 rows corresponding to the conservation constraints on each of three quantities in each of the four boxes within 18 layers. In each box, three additional constraints require that volume, heat, and salt be conserved, so $\mathbf{A}$ has a total of 228 rows. The term $\mathbf{b}$ is the vector representing bottom velocities b_i at all station pairs and interfacial velocities w between the layers, while $\mathbf{T}$ is a vector representing the total geostrophic and surface Ekman transports in each layer.

This standard inverse model is supplemented with additional constraints based on direct velocity measurements from ADCP measurements, ALACE floats, and altimeter-derived surface geostrophic velocities. For each available directly measured velocity d matched to station pair i, the model requires

$$b_i = d - v_i \quad \text{(A3)}$$

where b_i and v_i as above represent the unknown bottom velocity and the geostrophic velocity relative to the deepest common depth. For the ADCP measurements, $d - v_i$ and b_i are vertically integrated over 300 m to provide a less noisy comparison. The resulting inverse model is an augmented version of (A2):

$$\begin{pmatrix} \mathbf{A} \\ \mathbf{B} \end{pmatrix} \mathbf{b} = \begin{pmatrix} \mathbf{T} \\ \mathbf{D} \end{pmatrix} = \mathbf{A}'\mathbf{b} = \mathbf{T}', \quad \text{(A4)}$$

where $\mathbf{B}$ contains ones and zeros and $\mathbf{D}$ represents the right side of (A3), and $\mathbf{A}'$ and $\mathbf{T}'$ are augmented forms of $\mathbf{A}$ and $\mathbf{T}$, which include all of the direct velocity constraints. Thus in addition to conserving mass, heat, and salt the final solution will seek bottom velocities that minimize the differences between geostrophic velocities and the direct measurements. (Note that this approach is different from the one adopted by *Mercier et al.* [1993], who first bin-averaged their extensive North Atlantic float data set and then used the binned float measurements to constrain their nonlinear inverse model.)

A2. Establishing the Relative Weights of Measurements

The challenge in combining a suite of different direct velocities with hydrography is assigning relative weights to different measurements. To account for the differing accuracies of the data, each of the rows in (A4) is weighted by its expected rms error. This subsection summarizes how these row weights are selected.

A2.1. Hydrography. Hydrographic data are subject to errors due to instrument noise and ship drift during the course of the station casts. Together these could account for errors in geostrophic velocity relative to the bottom of the order of 0.005 m s^{-1}, but errors at adjacent stations will cancel each other out. A more serious source of error comes from the assumption that mass is conserved exactly within each of the boxes. Even for the short 4-month time interval of the reduced inverse model, mesoscale eddy processes can continually alter the volume of water in each box. This model resolves this inconsistency in the same way that previous inverse models have, by allowing a misfit of 2×10^9 kg s^{-1} in each layer and 1×10^9 kg s^{-1} for the vertically integrated budget [*Macdonald*, 1993]. These misfits correspond to rms vertical velocities of $O(10^{-6})$ m s^{-1} and rms bottom velocities of $O(10^{-4})$ m s^{-1} for the vertically integrated water column. For outcropping layers, hydrographic row weights are adjusted to include the estimated wind stress errors from CERSAT.

A2.2. Estimating ADCP errors. Uncertainties in ADCP constraints come from instrument error and from ageostrophic motion. The largest source of instrument error arises from the erroneous cross-track velocity due to

heading error, hence the importance of heading corrections and calibration. Except for a long segment of (P17-P19) when GPS attitude data were unavailable due to an antenna connection problem, gaps were typically < 1 hour. ADCP data were used in the inversion only for the 152 station pairs with better than 30% GPS attitude coverage (or 155 station pairs in the three-box model F which extended farther south on its westernmost section). Because ADCP data with serious navigational problems were eliminated, the cross-track error due to heading error for these pairs is expected to be < 0.01 m s^{-1} (K. Donohue, personal communication, 1998).

More serious sources of error in the ADCP-measured currents are caused primarily by near-inertial waves, internal tides, and barotropic tides. On the basis of the tide model of *Egbert et al.* [1994] and *Egbert* [1997] (version 3.0) the cross-track tide averaged between station pairs is typically about 0.02 m s^{-1}. Baroclinically varying errors were estimated by examining the variance of the on-station ADCP measurements (S. Chen, personal communication, 1998). On the basis of this analysis, total ADCP errors varied between 0.01 and 0.02 m s^{-1}.

A2.3. Temporal and spatial decorrelation of ALACE floats. Row weights for ALACE floats are influenced not only by instrumental errors but also by the fact that floats and CTD measurements are not collocated in time and space. While the long timescales of the ALACE measurements filter out transient velocities not seen by the CTD, over time the ALACE velocities decorrelate with geostrophic velocities inferred from a CTD. The expected squared difference between hydrographic (v_h) and ALACE (v_d) velocity estimates is

$$< (v_h - v_d)^2 >= 2 < v_h^2 > -2 < v_h v_d > \qquad \text{(A5)}$$

where angle brackets denote the expected or mean value and v_h and v_d are assumed to have the same variance. The covariance $< v_h v_d >$ is

$$\begin{aligned} < v_h v_d > &=< v_h >< v_d > + < v_h' v_d' > \\ &= \overline{R}(\Delta x) + R'(\Delta x, \Delta t) \end{aligned} \qquad \text{(A6)}$$

where primes represent temporal variability. The terms $\overline{R}$ and R' correspond to the time mean and time variable components of the autocovariance functions, respectively. These autocovariance functions are determined using the spatial and temporal autocovariance functions estimated by *Gille and Kelly* [1996] based on Geosat altimeter measurements in the Southern Ocean. Thus

$$\begin{aligned} \overline{R}(\Delta x) + R'(\Delta x, \Delta t) &= M_1 \exp\left[-\left(\frac{\Delta x}{L_x}\right)^2 - \left(\frac{\Delta y}{L_y}\right)^2\right] \\ &+ M_2 \exp\left[-\frac{(\Delta x)^2 + (\Delta y)^2}{l^2} - \left(\frac{\Delta t}{T}\right)\right] + M_3 \delta(i,j). \end{aligned} \qquad \text{(A7)}$$

Here the first term on the right represents the spatial covariance of the time-invariant components of velocity. Its zonal and meridional decorrelation length scales L_x and L_y are estimated to be 200 and 100 km, respectively. The second term on the right is the spatial and temporal covariance of the time-varying part of the velocities. Its decorrelation length scale l is set to 85 km, and the timescale T is 34 days. The final term on the right represents the fraction of velocity covariance due to measurement errors assumed to be uncorrelated in space or time. The function δ is zero except where the measurement indices, i and j, are identical, in which case the velocity variance is calculated. A more refined estimate of autocovariance that accounted for the duration of the ALACE float submergence was not attempted in this study.

The sum of the coefficients $M_1 + M_2 + M_3$ is the mean observed zero-lag velocity variance, $(< v_h^2 > + < v_d^2 >)/2$, in this case, 4×10^{-3} m^2 s^{-2}. A broad range of M_2 and M_3 were sampled to find the values for which $< (v_h - v_d)^2 >$ best matched its predicted covariance. Here M_2 is 4.2×10^{-4} m^2 s^{-2}, and M_3 is 3×10^{-4} m^2 s^{-2}. Combining (A5) and (A7),

$$\begin{aligned} < (v_h - v_d)^2 >= 2(M_1 + M_2 + M_3) \\ -2M_1 \exp\left[-\left(\frac{\Delta x}{L_x}\right)^2 - \left(\frac{\Delta y}{L_y}\right)^2\right] \\ -2M_2 \exp\left[-\frac{(\Delta x)^2 + (\Delta y)^2}{l^2} - \left(\frac{\Delta t}{T}\right)\right]. \end{aligned} \qquad \text{(A8)}$$

To test this, data were sorted and binned based on the predicted covariance estimates. Figure A1 shows reasonable agreement between the mean-squared-velocity difference from the left-hand side of (A8) and the predicted covariance from the right-hand side of (A8). To the extent that the points in Figure A1 fall along a straight line, the decorrelation function represented by (A8) provides a measure of the expected difference between hydrographic and ALACE-velocity estimates. This function is therefore used to establish row weightings for each of the ALACE/hydrographic pairs included in the inverse model.

A2.4. Altimeter errors. Reconstructed mean sea surface heights from altimetery are estimated to have rms errors of 0.10 m s^{-1} based on error analysis carried out using Monte Carlo simulations [*Gille*, 1994]. These large values mean that the altimeter measurements only slightly influence the inverse model solution.

A2.5. Checking the weights. Once the row weights were established, the inverse model matrix **A** was column weighted by the norm of its columns. This weighting was chosen rather than the area norm to avoid letting station pairs with many direct velocity measurements overly influence the solution.

For the inverse model as a whole and for each data type, after the inverse solution was computed, the choice of error magnitudes was verified with a chi-square test [*Wunsch*, 1996]. The number of singular values used is determined by requiring that the misfit in (A4) match the anticipated errors,

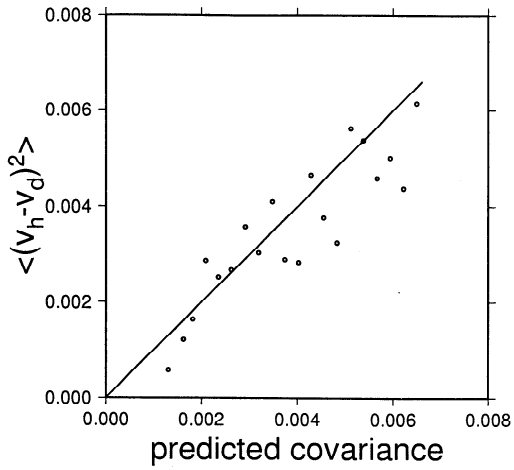

Figure A1. Comparison of the predicted and actual mean-squared difference between hydrographic and ALACE velocity measurements. The x coordinate of the circles is the predicted covariance based on the right-hand side of (A8), while the y coordinate indicates the observed mean-squared velocity difference. If predictions and observations matched exactly, the points would fall on the solid line with slope one. To generate this figure, the data are binned based on their predicted covariance, and each circle represents an average of $\sim$ 50 velocity pairs. No bottom velocity has been added to the hydrographic measurements, but it is assumed to be small compared with the other factors (such as spatial and temporal decorrelation) that account for differences between the two velocity estimates.

so that

$$\sum_{j=1}^{N} \frac{(T'_j - \mathbf{A'}_{ij}\mathbf{b}_i)^2}{\sigma_j^2} \approx N - m \qquad \text{(A9)}$$

where σ_j is the row weight, N is the number of rows, and m is the number of singular values employed in determining the solution $\mathbf{b}$. In addition, for each category of data, the mean row-weighted misfit should be $\sim$ 1. In cases where error estimates and final misfits could not be made to match to within about 10%, predicted error bars were adjusted and the inverse solution was recomputed.

Once the number of singular values m has been selected, formal error estimates are defined as

$$\mathbf{P} = \sum_{i=1}^{m} \frac{\mathbf{v}_i\mathbf{v}_i}{\lambda_i^2} + \sum_{i=m+1}^{M} \alpha^2 \mathbf{v}_i\mathbf{v}_i \qquad \text{(A10)}$$

where $\mathbf{v}_i$ are the singular vectors from the "right-hand" side of the singular value decomposition, λ_i are the singular values, M is the total number of singular values, and α is a constant used to scale the error estimates for the solution nullspace [*Wunsch*, 1996]. The constant α is necessarily unknown and is arbitrarily set to be roughly $1/\lambda_m^2$. Because the magnitude of the nullspace error is unknown, formal errors are an approximation.

Acknowledgments. Kathy Donohue provided invaluable advice on the ADCP data and on the manuscript itself. Joe Reid, Jim Swift, Greg Johnson, Eric Firing, and Russ Davis kindly allowed use of their data from the WOCE P16-17, P17-19, and P18 cruises. This research and its presentation have profited from comments from Russ Davis, Eric Firing, Joe Reid, Paul Robbins, Bernadette Sloyan, Lynne Talley, and the anonymous reviewers. The Jet Propulsion Laboratory (JPL) provided the TOPEX/Poseidon altimeter data used in this analysis. Funding was provided by NOAA grant NA47GP0188 to the Lamont/Scripps Consortium for Climate Research, by JPL contract 960875 with Scripps Institution of Oceanography, and by the North Atlantic Treaty Organization under a grant awarded in 1997.

References

Barnier, B., L. Siefridt, and P. Marchesiello, Thermal forcing for a global ocean circulation model using a three-year climatology of ECMWF analyses, *J. Mar. Syst.*, *6*, 363–380, 1995.

Bennett, A. F., Poleward heat fluxes in Southern Hemisphere oceans, *J. Phys. Oceanogr.*, *8*, 785–798, 1978.

Bentamy, A., N. Grima, Y. Quilfen, V. Harscoat, C. Maroni, and S. Pouliquen, An atlas of surface wind from ERS-1 scatterometer measurements, IFREMER, Plouzané, France, 229 pp., 1996.

Bingham, F. M., and L. D. Talley, Estimates of Kuroshio transport using an inverse technique, *Deep Sea Res. Part A*, *38S*, 21–43, 1991.

Carmack, E. C., Large-scale physical oceanography of polar oceans, in *Polar Oceanography: Part A, Physical Science*, edited by W. O. Smith, pp. 171–222, Academic, San Diego, Calif., 1990.

Davis, R. E., Preliminary results from directly measuring middepth circulation in the tropical and South Pacific, *J. Geophys. Res.*, *103*, 24,619–24,639, 1998.

deSzoeke, R. A., and M. D. Levine, The advective flux of heat by mean geostrophic motions in the Southern Ocean, *Deep Sea Res.*, *28*, 1057–1085, 1981.

Döös, K., and D. J. Webb, The Deacon Cell and the other meridional cells of the Southern Ocean, *J. Phys. Oceanogr.*, *24*, 429–442, 1994.

Egbert, G. D., Tidal data inversion: Interpolation and inference, *Prog. in Oceanogr.*, *40*, 53–80, 1997.

Egbert, G. D., A. F. Bennett, and M. G. G. Foreman, TOPEX/Poseidon tides estimated using a global inverse model, *J. of Geophys. Res.*, *99*, 24821–24852, 1994.

Firing, E., Acoustic Doppler current profiling measurements and navigation, *US World Ocean Circ. Exp. Hydrogr. Prog. Rep. WHPO-91-1, WOCE rep. 68/91*, San Diego, Calif., 1991.

Georgi, D. T., and J. M. Toole, The Antarctic Circumpolar Current and the oceanic heat and freshwater budgets, *J. Mar. Res.*, *40S*, 183–197, 1982.

Gille, S. T., Mean sea surface height of the Antarctic Circumpolar Current from Geosat data: Method and application, *J. Geophys. Res.*, *99*, 18,255–18,273, 1994.

Gille, S. T., and K. A. Kelly, Scales of spatial and temporal variability in the Southern Ocean, *J. Geophys. Res.*, *101*, 8759–8773, 1996.

Gordon, A. L., Seasonality of Southern Ocean sea ice, *J. Geophys. Res.*, *86*, 4193–4198, 1981.

Gordon, A. L., and W. B. Owens, Polar oceans, *Rev. Geophys.*, *25*, 227–233, 1987.

Hastenrath, S., Heat budget of tropical ocean and atmosphere, *J. Phys. Oceanogr.*, *10*, 159–170, 1980.

Hastenrath, S., On meridional heat transports in the world ocean, *J. Phys. Oceanogr.*, *12*, 922–927, 1982.

Hsiung, J., Estimates of global oceanic meridional heat transport, *J. Phys. Oceangr.*, *15*, 1405–1413, 1985.

Jackett, D. R., and T. J. McDougall, A neutral density variable for the world's oceans, *J. Phys. Oceanogr.*, *27*, 237–263, 1997.

Johnson, G. C., and H. L. Bryden, On the size of the Antarctic Circumpolar Current, *Deep Sea Res.*, *36*, 39–53, 1989.

Joyce, T. M., On in situ calibration of shipboard ADCPs, *J. Atmos. Oceanic Technol.*, *6*, 169–172, 1989.

Joyce, T. M., C. Wunsch, and S. D. Pierce, Synoptic Gulf Stream velocity profiles through simultaneous inversion of hydrographic and acoustic Doppler data, *J. Geophys. Res.*, *91*, 7573–7585, 1986.

Keffer, T., and G. Holloway, Estimating Southern Ocean eddy flux of heat and salt from satellite altimetry, *Nature*, *332*, 624–626, 1988.

King, B. A., and E. B. Cooper, Comparison of ship's heading determined from an array of GPS antennas with heading from conventional gyrocompass measurements, *Deep Sea Res., Part I*, *40*, 2207–2216, 1993.

Macdonald, A. M., Property fluxes at 30°S and their implications for the Pacific-Indian throughflow and the global heat budget, *J. Geophys. Res.*, *98*, 6851–6868, 1993.

Macdonald, A. M., and C. Wunsch, An estimate of global ocean circulation and heat fluxes, *Nature*, *382*, 436–439, 1996.

McCartney, M. S., Subantarctic mode water, *Deep Sea Res.*, *24*, 103–119, 1977.

McIntosh, P. C., and S. R. Rintoul, Do box inverse models work?, *J. Phys. Oceanogr.*, *27*, 291–308, 1997.

Mercier, H., M. Ollitrault, and P. Y. Le Traon, An inverse model of the North Atlantic general circulation using Lagrangian float data, *J. Phys. Oceanogr.*, *23*, 689–715, 1993.

Olbers, D., V. Gouretski, G. Seiß, and J. Schröter, *Hydrographic Atlas of the Southern Ocean*. Alfred Wegener Inst., Bremerhaven, Germany, 1992.

Orsi, A. H., T. Whitworth III, and W. D. Nowlin Jr., On the meridional extent and fronts of the Antarctic Circumpolar Current, *Deep Sea Res., Part I*, *42*, 641–673, 1995.

Pollard, R., and J. Read, A method for calibrating shipmounted acoustic Doppler profilers and the limitations of gyro compasses, *J. Atmos. Oceanic Technol.*, *6*, 859–865, 1989.

Polzin, K. L., J. M. Toole, J. R. Ledwell, and R. W. Schmitt, Spatial variability of turbulent mixing in the abyssal ocean, *Science*, *276*, 93–96, 1997.

Reid, J. L., On the total geostrophic circulation of the South Pacific Ocean: Flow patterns, tracers and transports, *Prog. Oceanogr.*, *16*, 1–61, 1986.

Rintoul, S. R., South Atlantic interbasin exchange, *J. Geophys. Res.*, *96*, 2675–2692, 1991.

Sandwell, D. T., and B. Zhang, Global mesoscale varability from Geosat Exact Repeat Mission: Correlation with ocean depth, *J. Geophys. Res.*, *94*, 17,971–17,984, 1989.

Sloyan, B. M., The circulation of the Southern Ocean and the adjacent ocean basins determined by inverse methods, Ph.D. thesis, Inst. of Antarct. and South. Ocean Stud., Univ. of Tasmania, Hobart, 1997.

Stammer, D., On eddy characteristics, eddy transports, and mean flow properties, *J. Phys. Oceanogr.*, *28*, 727–739, 1998.

Talley, L. D., Meridional heat transport in the Pacific Ocean, *J. Phys. Oceanogr.*, *14*, 231–241, 1984.

Warren, B. A., Suppression of deep oxygen concentrations by Drake Passage, *Deep Sea Res., Part A*, *37*, 1899–1907, 1990.

Whitworth, III, T., W. D. Nowlin, Jr., and S. J. Worley, The net transport of the Antarctic Circumpolar Current through Drake Passage, *J. Phys. Oceanogr.*, *12*, 960–971, 1982.

Wrigley, W., W. M. Hollister, and W. G. Denhard, *Gyroscopic Theory, Design and Instrumentation*. MIT Press, Cambridge, Mass., 1969.

Wunsch, C., *The Ocean Circulation Inverse Problem*,. Cambridge Univ. Press, New York, 1996.

Wunsch, C., D. Hu, and B. Grant, Mass, heat, salt and nutrient flux in the South Pacific Ocean, *J. Phys. Oceanogr.*, *13*, 725–753, 1983.

Sarah T. Gille, Department of Earth System Science, University of California, Irvine, CA 92697-3100. (sgille@uci.edu)

(Received December 23, 1997; revised December 3, 1998; accepted December 9, 1998.)